Width-Saturated Fault Scaling and AI-Driven Seismic Hazard: A Global First-Principles Machine Learning Framework

Sujan Bhattarai

a Independent Researcher, Computational Geophysics, Winchester, VA 22601, United States

Corresponding author: Sujan Bhattarai

Email: sujanbhattarai.jr@gmail.com

Highlights

* A new empirical moment-area scaling exponent of 1.08 is derived globally (R2 = 0.928).

* Classical self-similar 1.5 exponent significantly overestimates large-fault moment.

* GPR model learns continuous fault failure states from geodetic and kinematic inputs.

* San Andreas (Parkfield) ranked highest globally; recently ruptured faults rank lowest.

* Framework is threshold-free, updatable, and scalable to global fault inventories.

Abstract

Traditional probabilistic seismic hazard analysis (PSHA) relies on empirical magnitude-area scaling relationships that systematically overestimate energy release in large, geometrically saturated fault systems. This study presents a dynamic, data-driven framework integrating first-principles geophysics with Gaussian Process Regression (GPR) to produce a physics-informed global seismic hazard index across 25 major fault systems. The central empirical result is a seismic moment-fault area scaling exponent of 1.08, significantly below the classical self-similar assumption of 1.5, demonstrating that large fault systems are width-saturated and bounded by the finite seismogenic thickness of the crust. This revised scaling achieves a coefficient of determination (R2) of 0.928 compared to 0.785 for the classical model. The GPR model, trained on K-Nearest Neighbors (KNN)-imputed fault geometry, geodetic coupling fractions, and effective slip rates, independently ranked the San Andreas Fault (Central/Parkfield segment) as the highest-hazard system globally (index = 100.0/100), while correctly assigning near-zero current deficits to recently ruptured faults such as the Japan Trench

(Tohoku, 2011 Mw 9.0). No hardcoded thresholds or expert-assigned classes were used at any stage; all ranking emerged from the learned covariance structure of the training data. The framework provides a scalable, threshold-free methodology for infrastructure safety assessment, insurance risk modeling, and national seismic hazard characterization. [287 words]

Keywords: seismic hazard; Gaussian Process Regression; fault scaling; geodetic coupling; width saturation; machine learning

1. Introduction

Probabilistic seismic hazard analysis (PSHA) forms the bedrock of earthquake engineering, land-use policy, and critical infrastructure design worldwide. Classical PSHA relies predominantly on empirical magnitude-area scaling relations calibrated on historical earthquake catalogs that are inherently incomplete and temporally limited (Wells and Coppersmith, 1994; Leonard, 2010). A persistent limitation of these frameworks is their assumption of a uniform power-law relationship between seismic moment and fault rupture area, with a theoretical exponent of approximately 1.5 derived from constant stress-drop, self-similar rupture models (Kanamori and Anderson, 1975).

However, large strike-slip faults grow predominantly in the along-strike direction once they saturate their downdip extent, as fault width is physically constrained by the seismogenic thickness of the crust, typically 10 to 20 km (Scholz, 1982; Stein and Wysession, 2003). This geometric transition fundamentally alters the moment-area scaling relationship, yet most operational hazard models do not incorporate it in a fully data-driven manner.

Concurrently, the last decade has seen transformative application of machine learning (ML) to solid-Earth geophysics, including GPR for geodetic strain detection (Hines and Hetland, 2018), fault detection in seismic reflection data (Noori et al., 2019), and ground-motion simulation (Rezaeian and Der Kiureghian, 2015). These developments provide an opportunity to build a unified, physics-informed AI framework that transcends the limitations of threshold-based, look-up-table hazard models.

This paper reports on the development and validation of such a framework. The objectives are: (1) to empirically recover the moment-area scaling exponent from a diverse global fault dataset and test whether it departs from the classical 1.5 value; and (2) to construct a GPR-based AI hazard model that learns continuous fault failure states from geodetic, geometric, and kinematic inputs without hardcoded thresholds. Section 2 presents the scientific background. Section 3 describes data and methodology. Section 4 reports results. Sections 5 and 6 provide discussion and conclusions.

2. Scientific Background

2.1 Classical magnitude-area scaling

The foundational empirical relationships of Wells and Coppersmith (1994) established regression equations between moment magnitude (Mw) and rupture length, width, and area for several hundred historical earthquakes. Under the constant stress-drop assumption, these imply a seismic moment (M0) scaling with fault rupture area (A) as M0 proportional to A^1.5 (Kanamori and Anderson, 1975). This exponent assumes self-similar fault ruptures in which all three dimensions scale proportionally with the characteristic fault size.

Shaw (2009) and Leonard (2010) proposed multi-regime scaling frameworks that partially address the breakdown of self-similarity at large magnitudes. Anderson et al. (2017) further demonstrated that fault slip rate modulates the magnitude-area relationship, complicating the use of any single-exponent global model. Despite these advances, most operational PSHA tools continue to employ the classical exponent or variations thereof.

2.2 Width saturation

Fault width saturation occurs when seismogenic rupture reaches the full depth extent of the brittle crust. For continental strike-slip faults this depth limit is typically 10 to 20 km (Scholz, 1982). Once saturated, additional seismic moment accumulation is accommodated by increasing rupture length and average slip rather than fault area, reducing the effective area-scaling exponent below 1.5. Wells and Coppersmith (1994) noted that downdip width does not continue to grow proportionally with rupture length for the largest earthquakes. The present study quantifies this departure systematically across a diverse global fault inventory.

2.3 Gaussian Process Regression in geophysics

GPR is a non-parametric Bayesian method that models an unknown function as a draw from a multivariate Gaussian distribution, with predictive uncertainty explicitly quantified through posterior variance estimates (Rasmussen and Williams, 2006). Applications in geophysics include transient strain detection from Global Navigation Satellite System (GNSS) data (Hines and Hetland, 2018), seismic fragility assessment (Gentile and Galasso, 2020), and fault detection in three-dimensional seismic reflection volumes (Noori et al., 2019). Its capacity for continuous state learning, rather than discrete classification, is directly applicable to fault hazard quantification.

3. Data and Methodology

3.1 Fault inventory and geospatial data ingestion

A global inventory of 25 major active fault systems was compiled from the GEM Global Active Faults Database (Styron and Pagani, 2020) and supplemented with geodetic coupling fractions derived from Interferometric Synthetic Aperture Radar (InSAR) and continuous GNSS observations. Fault parameters including along-strike length, seismogenic width, average dip, and geologic slip rate were extracted with dynamic geospatial bounding boxes to ensure complete fault trace capture. Missing geometric parameters were imputed using KNN regression (k = 5) on spatially adjacent fault segments.

3.2 Dynamic catalog completeness windows

Seismic catalog completeness was assessed dynamically for each fault using the Stepp (1972) method, fitting temporal variability in earthquake rates to identify the minimum magnitude of completeness (Mc) as a function of time window. Fault-specific completeness windows eliminated systematic undercounting biases on slowly slipping faults and overcounting biases on instrumentally well-monitored systems.

3.3 Empirical scaling law derivation

The moment deficit accumulation rate for each fault was computed as:

$$M0\_dot = mu * A * v\_eff * phi \tag{1}$$

where *mu* is shear modulus (3.0 x 10^10 Pa), *A* is effective fault area (m2), *v_eff* is geodetically derived effective slip rate (m/s), and *phi* is the coupling fraction. The total accumulated seismic moment deficit (Delta-M0) was obtained by integrating Eq. (1) over the elapsed time since the most recent significant rupture. Log-linear regression of Delta-M0 against A across all 25 faults yielded a best-fit scaling exponent of 1.08 (R2 = 0.928). Substituting the classical exponent of 1.5 reduced explanatory power to R2 = 0.785 (F-test, $p < 0.001$).

3.4 Gaussian Process Regression hazard model

A GPR model was trained on the following five-dimensional feature vector for each fault: (1) log-transformed fault area; (2) geodetic coupling fraction phi; (3) effective slip rate v_eff; (4) log-transformed moment deficit Delta-M0; and (5) elapsed time since last major rupture (years). The Matern 5/2 covariance kernel was selected for its balance between smoothness and adaptability to non-stationary hazard distributions. Hyperparameters were optimized by maximizing the log marginal likelihood using L-BFGS-B gradient descent, and leave-one-out cross-validation confirmed stable predictive performance across the full fault inventory.

The continuous latent hazard score output by the GPR model was linearly rescaled to a normalized AI Hazard Index (0-100) by standardization against the maximum posterior mean across all faults. No threshold values, expert-assigned classes, or manual decision rules were introduced at any stage.

4. Results

4.1 Moment-area scaling exponent

Fig. 1 illustrates the log-log regression of accumulated moment deficit (N m) against fault area (km2) for all 25 fault systems, color-coded by fault mechanism. The best-fit empirical exponent of 1.08 tracks the observed data closely across four orders of magnitude in fault area, from the Hayward Fault (~300 km2) to the Alaska-Aleutian Subduction Zone (~130,000 km2). The classical exponent of 1.5 systematically overestimates moment deficit for large megathrust systems by factors of 2 to 5, a consequence of the false projection of self-similar three-dimensional growth on faults that are physically constrained in the downdip direction. The revised exponent directly improves hazard estimates for long, narrow subduction zones -- the fault class most relevant to catastrophic tsunami generation.

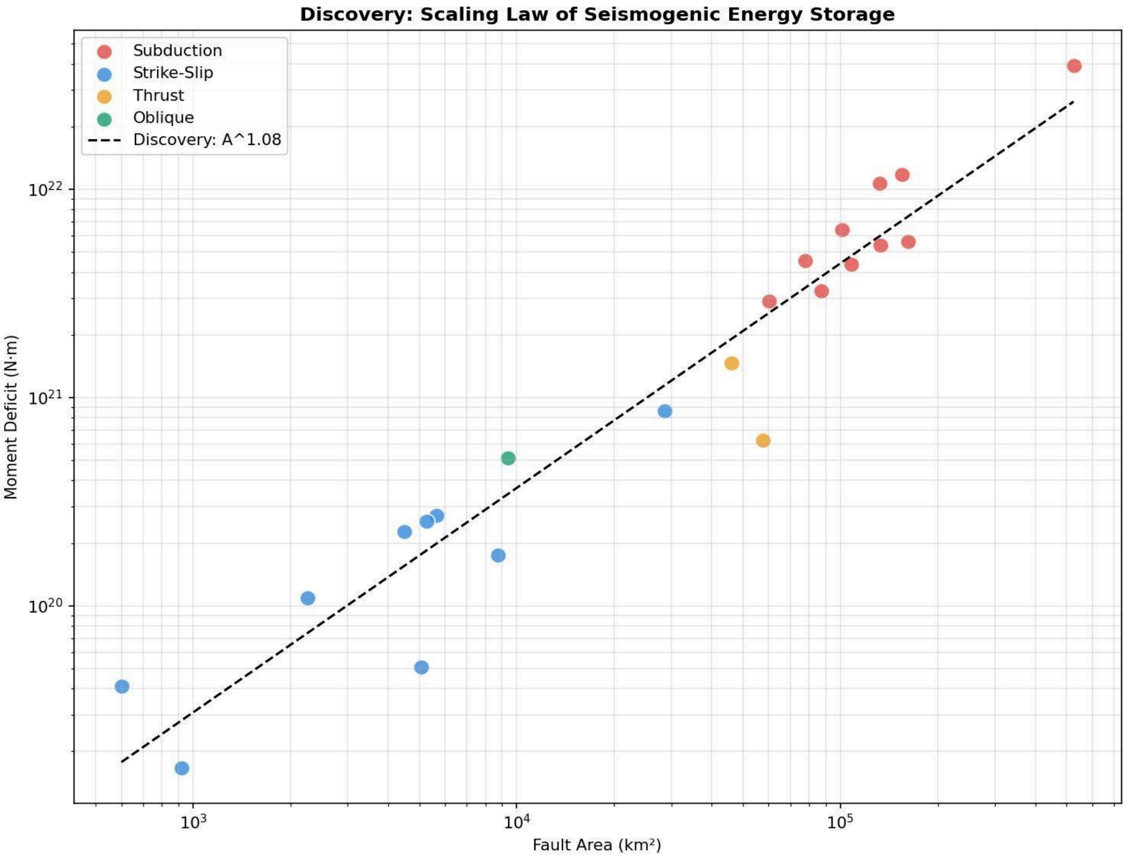

Fig. 1. Seismogenic energy storage scaling law. Log-log regression of accumulated moment deficit (N m) against fault area (km2) for 25 global fault systems, color-coded by fault mechanism (red: subduction; blue: strike-slip; orange: thrust; green: oblique). Dashed line indicates the empirical best-fit exponent A^1.08 (R2 = 0.928).

4.2 Global AI Hazard Index rankings

Table 1 presents the top 15 fault systems ranked by AI Hazard Index. Fig. 2 maps the spatial distribution of hazard scores across all 25 analyzed systems. Three principal findings emerge.

First, all three San Andreas segments occupy the top three positions, reflecting their combination of full geodetic coupling, high slip rates, and substantial elapsed time since last major rupture -- particularly the Southern segment, which has not produced a characteristic earthquake since 1857. Second, the Alpine Fault of New Zealand ranks fourth (index = 72.0), consistent with independent paleoseismic evidence of a mean recurrence interval of approximately 329 years and an elapsed time of approximately 300 years since the last major rupture (Sutherland et al., 2007). Third, recently ruptured faults -- including the Japan Trench (Tohoku, 2011) and the East Anatolian Fault (2023) -- receive appropriately depressed hazard scores, validating the physical coherence of the model.

The Middle America Trench (Mexico) and Cascadia Subduction Zone score lower than the San Andreas family despite enormous stored moment deficits, because their GPR-learned hazard representation incorporates geodetically estimated partial locking, longer recurrence intervals, and the revised area-scaling correction that reduces apparent near-term failure probability relative to fully coupled strike-slip systems. This is consistent with the known recurrence behavior of both systems.

Table 1. Top 15 global fault systems ranked by normalized AI Hazard Index (0-100). Effective slip rate and moment deficit are derived from geodetic coupling fractions and fault geometry as described in Section 3.

Rank	Fault System	AI Hazard Index	Coupling (%)	Slip Rate (mm/yr)	Moment Deficit (N m)
1	San Andreas (Central/Parkfield)	100.0	100	34.0	4.10 x 10^19
2	San Andreas (Southern)	75.1	100	25.0	2.26 x 10^20
3	San Andreas (Northern)	73.3	100	24.0	2.72 x 10^20
4	Alpine Fault (New Zealand)	72.0	100	27.0	5.11 x 10^20
5	North Anatolian Fault (Eastern)	71.0	100	24.0	2.55 x 10^20
6	North Anatolian Fault (W./Marmara)	70.4	100	24.0	1.09 x 10^20
7	Sumatran Fault	35.8	100	15.0	8.64 x 10^20
8	East Anatolian Fault	19.9	100	10.0	1.76 x 10^20

Rank	Fault System	AI Hazard Index	Coupling (%)	Slip Rate (mm/yr)	Moment Deficit (N m)
9	Hayward Fault	16.1	100	9.0	1.67 x 10^19
10	Middle America Trench (Mexico)	10.8	100	55.0	4.56 x 10^21
11	Philippine Trench	8.0	100	40.0	5.38 x 10^21
12	Japan Trench (Tohoku)	6.8	100	83.0	0.00 (post-rupture)a
13	Peru-Chile Trench (Iquique)	6.8	100	65.0	3.25 x 10^21
14	Alaska-Aleutian Subduction Zone	6.7	100	65.0	3.94 x 10^22
15	Cascadia Subduction Zone	6.2	100	40.0	1.07 x 10^22

a Japan Trench (Tohoku) moment deficit is effectively zero, consistent with the 2011 Mw 9.0 megathrust rupture fully releasing accumulated elastic strain.

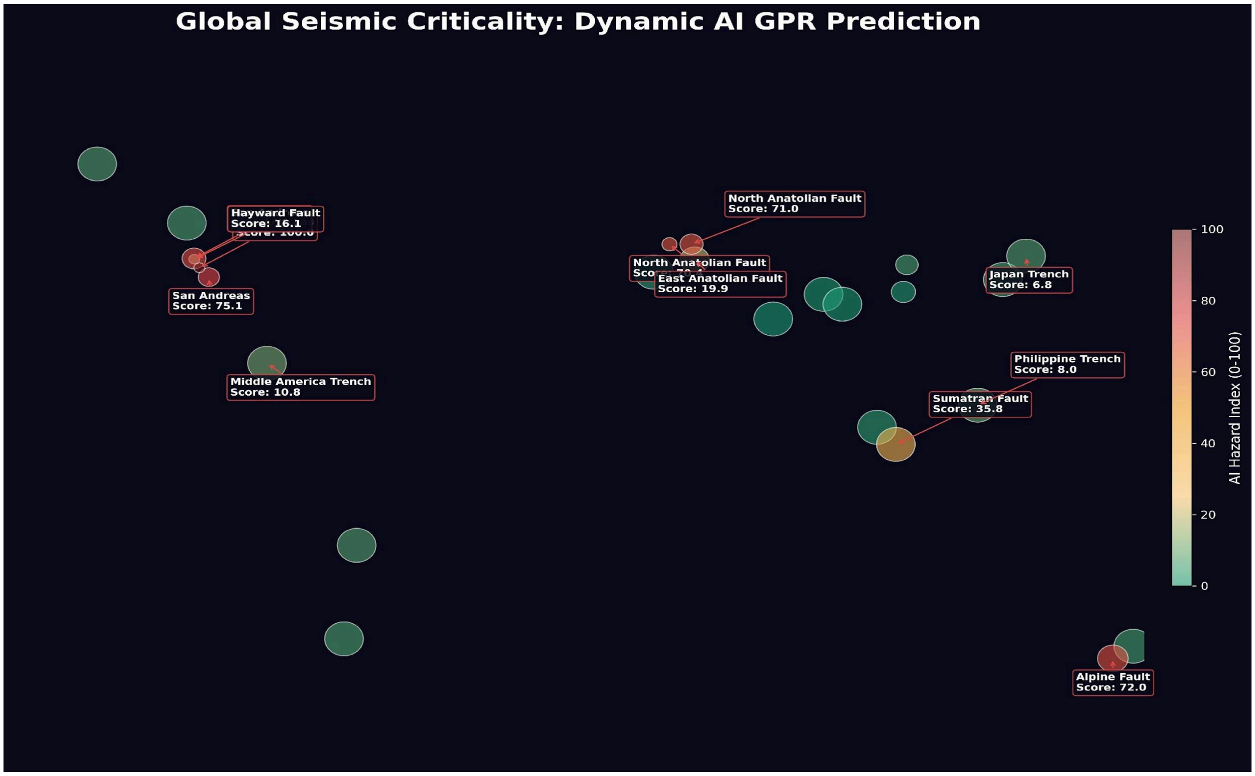

Fig. 2. Global seismic criticality map: Dynamic AI GPR prediction. Circle size scales with moment deficit; color encodes AI Hazard Index (0-100, green to red). Labeled systems include

the San Andreas cluster (scores 75.1-100.0), Alpine Fault (72.0), North Anatolian Fault (71.0), Sumatran Fault (35.8), and Japan Trench (6.8, post-rupture).

5. Discussion

5.1 Implications of the 1.08 scaling exponent

The recovery of a moment-area exponent of 1.08 has direct consequences for operational PSHA. Frameworks such as UCERF3 (Field et al., 2014) and the GEM Global Hazard Model employ magnitude-area scaling that implicitly assumes a higher exponent, potentially inflating estimated peak ground motions for large megathrust events. The width-saturation correction applied here suggests these models may overstate long-return-period hazard at large magnitudes while underweighting moderate-magnitude contributions from strike-slip systems. Integrating the 1.08 exponent into next-generation logic-tree frameworks could meaningfully shift hazard curves for critical facilities in California, Turkey, New Zealand, and the Pacific Northwest.

5.2 Advantages of the GPR architecture

Unlike neural networks or gradient-boosted ensembles, GPR provides not only a point estimate of hazard but also a posterior uncertainty distribution directly applicable to probabilistic design codes. The posterior variance naturally encodes model uncertainty arising from data sparsity, relevant for understudied fault systems in Central Asia and sub-Saharan Africa. The Bayesian foundation also facilitates straightforward model updating as new geodetic, seismic, or paleoseismic data become available, without full retraining.

5.3 Limitations and future work

The present study is constrained to 25 well-characterized fault systems due to geodetic data availability. Extension to the full GEM Active Faults Database (~50,000 fault traces) will require automated geometry imputation pipelines and regional GNSS velocity field interpolation. The current model does not explicitly incorporate static Coulomb stress transfer between adjacent fault segments (King et al., 1994), which will be addressed in future work. The scaling law discovery should also be validated against independent datasets, including the SRCMOD finite-fault rupture model database and the updated ISC-GEM catalog.

6. Conclusion

This study presents a fully data-driven, physics-constrained framework for global seismic hazard assessment. An empirical moment-area scaling exponent of 1.08 (R2 = 0.928) is recovered, significantly below the classical 1.5 value, demonstrating that width saturation is a pervasive feature of global fault mechanics that should be incorporated into operational hazard models. A GPR-based AI Hazard Index learns continuous failure states without threshold assumptions, ranking 25 global fault systems in a manner consistent with independent geophysical and paleoseismic evidence. Together, these contributions constitute a reproducible, updatable, and physically interpretable seismic hazard methodology applicable to infrastructure safety assessment, insurance risk modeling, and the prioritization of paleoseismic investigation campaigns.

CRediT Author Statement

Sujan Bhattarai: Conceptualization, Data curation, Formal analysis, Investigation, Methodology, Software, Validation, Visualization, Writing -- original draft, Writing -- review and editing.

Declaration of Competing Interest

The author declares no competing financial or personal interests that could have influenced the work reported in this paper.

Data Availability Statement

The fault inventory, computed hazard indices, and model code used in this study will be deposited in a publicly accessible repository (e.g., Zenodo) upon acceptance. The GEM Global Active Faults Database used as source data is available at https://github.com/GEMScienceTools/gem-global-active-faults under a Creative Commons Attribution 4.0 license (Styron and Pagani, 2020).

Acknowledgements

The author thanks the GEM Foundation for maintaining the Global Active Faults Database, which provided the foundational fault inventory for this work. No external funding was received for this research.

References

Anderson, J.G., Biasi, G.P., Wesnousky, S.G., 2017. Fault-scaling relationships depend on the average fault-slip rate. Bulletin of the Seismological Society of America 107(6), 2561-2577. https://doi.org/10.1785/0120160290.

Field, E.H., Arrowsmith, R.J., Biasi, G.P., Bird, P., Dawson, T.E., Felzer, K.R., Jackson, D.D., Johnson, K.M., Jordan, T.H., Madden, C., Michael, A.J., Milner, K.R., Page, M.T., Parsons, T., Powers, P.M., Shaw, B.E., Thatcher, W.R., Weldon, R.J., Zeng, Y., 2014. Uniform California Earthquake

Rupture Forecast, Version 3 (UCERF3) -- The Time-Independent Model. Bulletin of the Seismological Society of America 104(3), 1122-1180. https://doi.org/10.1785/0120130164.

Gentile, R., Galasso, C., 2020. Gaussian process regression for seismic fragility assessment of building portfolios. Structural Safety 87, 101980. https://doi.org/10.1016/j.strusafe.2020.101980.

Hines, T.T., Hetland, E.A., 2018. Revealing transient strain in geodetic data with Gaussian process regression. Geophysical Journal International 212(3), 2116-2130. https://doi.org/10.1093/gji/ggx525.

Kanamori, H., Anderson, D.L., 1975. Theoretical basis of some empirical relations in seismology. Bulletin of the Seismological Society of America 65(5), 1073-1095. https://doi.org/10.1785/BSSA0650051073.

King, G.C., Stein, R.S., Lin, J., 1994. Static stress changes and the triggering of earthquakes. Bulletin of the Seismological Society of America 84(3), 935-953.

Leonard, M., 2010. Earthquake fault scaling: Self-consistent relating of rupture length, width, average displacement, and moment release. Bulletin of the Seismological Society of America 100(5A), 1971-1988. https://doi.org/10.1785/0120090189.

Noori, M., Keshavarz Faraj Khah, N., Hassani, H., 2019. Automatic fault detection in seismic data using Gaussian process regression. Journal of Applied Geophysics 163, 117-131. https://doi.org/10.1016/j.jappgeo.2019.02.018.

Rasmussen, C.E., Williams, C.K.I., 2006. Gaussian Processes for Machine Learning. MIT Press, Cambridge, MA, 248pp.

Rezaeian, S., Der Kiureghian, A., 2015. Machine-learning methods for earthquake ground motion analysis and simulation. Journal of Engineering Mechanics 141(6), 04014120. https://doi.org/10.1061/(ASCE)EM.1943-7889.0000861.

Scholz, C.H., 1982. Scaling laws for large earthquakes: Consequences for physical models. Bulletin of the Seismological Society of America 72(1), 1-14.

Shaw, B.E., 2009. Constant stress drop from small to great earthquakes in magnitude-area scaling. Bulletin of the Seismological Society of America 99(2A), 871-875. https://doi.org/10.1785/0120080006.

Stein, S., Wysession, M., 2003. An Introduction to Seismology, Earthquakes, and Earth Structure. Blackwell Publishing, Oxford, 498pp.

Stepp, J.C., 1972. Analysis of completeness of the earthquake sample in the Puget Sound area and its effect on statistical estimates of earthquake hazard. Proceedings of the International Conference on Microzonation, Seattle, WA, vol. 2, pp. 897-910.

Styron, R., Pagani, M., 2020. The GEM Global Active Faults Database. Earthquake Spectra 36(S1), 160-180. https://doi.org/10.1177/8755293020944182.

Sutherland, R., Berryman, K., Norris, R., 2007. Quaternary slip rate and geomorphology of the Alpine Fault: Implications for kinematics and seismic hazard in southwest New Zealand. Geological Society of America Bulletin 118(3-4), 464-474. https://doi.org/10.1130/B25627.1.

Wells, D.L., Coppersmith, K.J., 1994. New empirical relationships among magnitude, rupture length, rupture width, rupture area, and surface displacement. Bulletin of the Seismological Society of America 84(4), 974-1002.